Research Square

Preprints are preliminary reports that have not undergone peer review.
They should not be considered conclusive, used to inform clinical practice,
or referenced by the media as validated information.

Nonlinear Dynamics and Resonance Analysis of an Electromagnetically Controlled Rotor System Using HQM-Based Continuation

Farouk Thaljaoui

faroukmecanique@gmail.com

University of Carthage

Thabet Gasmi

University of Gafsa

Wathek Thaljaoui

University of Sousse

Research Article

Keywords: Nonlinear rotor dynamics, Continuation techniques, Electromagnetic coupling, Bifurcation analysis

Posted Date: June 25th, 2026

DOI: https://doi.org/10.21203/rs.3.rs-10025244/v1

License: This work is licensed under a Creative Commons Attribution 4.0 International License.
Read Full License

Additional Declarations: No competing interests reported.

Nonlinear Dynamics and Resonance Analysis of an Electromagnetically Controlled Rotor System Using HQM-Based Continuation

Farouk Thaljaoui[1,2*], Thabet Guesmi[3,4†] and Wathek Thaljaoui[5,6†]

[1*]Department of Mechanical Engineering, Tunisia Polytechnic School, University of Carthage, B.P.743, La Marsa, 2078, Tunis, Tunisia.
[2]Applied Mechanics and Systems Research Laboratory, Tunisia Polytechnic School, University of Carthage, B.P.743, La Marsa, 10587, Tunis, Tunisia.
[3]Department of Physics, Faculty of Science of Gafsa, University of Gafsa, 2112, Gafsa, Tunisia.
[4]Laboratory of Technology, Energy and Innovative Materials, Faculty of Science of Gafsa, University of Gafsa, 2112, Gafsa, Tunisia.
[5]Department of Mechanical Engineering, Higher Institute of Technological Studies of Sidi Bouzid, B.P.377, 9100, Sidi Bouzid, Tunisia.
[6]Department of Forensic Sciences , Faculty of Medicine of Sousse, 4002, Sousse, Tunisia.

*Corresponding author(s). E-mail(s): farouk.thaljawi@gmail.com;
Contributing authors: gasmithabet.thabet@gmail.com;
thaljawiwathek@yahoo.fr;
†These authors contributed equally to this work.

Abstract

This study investigates the nonlinear dynamics of a flexible rotor supported by active magnetic bearings and subjected to proportional–derivative (PD) feedback control. The system response is analyzed over a wide range of operating conditions through bifurcation diagrams, fast Fourier transform spectra, Poincare sections, and phase portraits, revealing dynamical regimes including periodic, quasi-periodic, and chaotic oscillations. The routes to chaos are examined through representative transition scenarios, characterized by intermittency and boundary crisis mechanisms rather than classical period-doubling cascades.

Forced response curves are computed via an extended Harmonic Quadrature Method (HQM) combined with arc-length continuation, enabling robust tracking of stable and unstable solution branches and detection of fold bifurcations in strongly nonlinear regimes. The method is validated against three benchmark cases involving magnetic, hydrodynamic, and cubic nonlinearities, with convergence achieved at $\boldsymbol{H = 11}$ harmonics.

Parametric investigations show that the proportional gain $\boldsymbol{P}$ acts as a destabilizing parameter, inducing pronounced softening-type nonlinearity and expanding quasi-periodic and chaotic regions, with a maximum response amplitude of $\mathbf{1.317}$ at $\boldsymbol{\Omega = 0.37}$ for $\boldsymbol{P = 2.5}$. The derivative gain $\boldsymbol{D}$ introduces effective damping that progressively suppresses nonlinear distortions and restores single-periodic behavior, with instability regions vanishing entirely at $\boldsymbol{D = 0.5}$. The electromagnetic coupling coefficient $\boldsymbol{\alpha}$ modulates cross-axis nonlinear interaction, with higher values promoting multiple solution branches and extended quasi-periodic regimes.

The proposed HQM-based continuation framework is demonstrated to be an efficient and robust computational tool for analyzing complex nonlinear resonance phenomena in feedback-controlled rotor systems, offering practical guidelines for the design and tuning of electromagnetically controlled rotating machinery.

Keywords: Nonlinear rotor dynamics, Continuation techniques, Electromagnetic coupling, Bifurcation analysis

1 Introduction

Rotating machinery is widely used in turbomachinery, aerospace systems, high-speed compressors, and precision manufacturing. Increasing demands for higher rotational speeds, improved efficiency, and operational reliability require advanced vibration control strategies capable of ensuring stable performance under complex operating conditions. As a result, the nonlinear dynamic behavior of rotor systems has attracted considerable attention over the past decades.

Depending on system parameters and operating conditions, rotor systems may exhibit a wide range of nonlinear phenomena, including bifurcations, subharmonic oscillations, amplitude jumps, quasiperiodic responses, and chaotic motion. These behaviors are commonly observed in systems involving nonlinear restoring forces, external excitations, fluid–structure interactions, or active control mechanisms, and may significantly affect the dynamic performance and safety of rotating machinery [1–4].

Among the various vibration mitigation strategies, electromagnetic control systems and active magnetic bearings have attracted considerable attention due to their contactless operation, reduced friction, and high controllability. These systems offer attractive solutions for high-speed rotating machinery, where conventional bearing technologies may face operational limitations. However, the coupling between rotor motion, electromagnetic forces, and feedback control introduces strong nonlinearities into the system dynamics. As a result, electromagnetically controlled rotor

systems may exhibit complex behaviors such as nonlinear resonance, multistability, bifurcations, and chaotic oscillations, which can significantly affect performance and operational reliability [5–18].

To investigate such nonlinear phenomena, various numerical and semi-analytical techniques have been developed, including direct time integration [19, 20], shooting methods [21, 22], harmonic balance approaches [23, 24], continuation techniques, and finite element formulations. These methods have proven effective in predicting nonlinear responses and identifying bifurcation structures in rotating systems.

However, strongly nonlinear rotor systems involving multiple dynamic transitions and unstable solution branches still present significant computational challenges. In particular, difficulties arise near bifurcation points and resonance regions, where accurate tracking of disconnected or turning solution branches becomes essential for capturing the global dynamic response.

Among the available approaches, harmonic-domain techniques have demonstrated strong capability for efficiently computing nonlinear periodic responses and forced oscillations, while reducing the computational cost associated with time-domain simulations. These methods are particularly suitable for strongly nonlinear systems exhibiting multiple steady-state solutions and resonance phenomena. In this context, the Harmonic Quadrature Method (HQM) provides a simple and efficient framework for the analysis of nonlinear dynamical systems. Its main advantage lies in its straightforward implementation, where the governing differential equations are transformed into algebraic equations, thereby simplifying the solution procedure. Unlike classical Galerkin-based harmonic balance methods, HQM avoids the evaluation of Galerkin integrals, which reduces both analytical complexity and computational effort. Consequently, HQM offers an efficient and accurate approach for computing periodic solutions and capturing nonlinear resonance characteristics.

Despite the extensive literature devoted to nonlinear rotor dynamics and electromagnetic control systems, the combined influence of proportional–derivative (PD) feedback and electromagnetic coupling on bifurcation structures, routes to chaos, and nonlinear resonance behavior remains insufficiently investigated. Furthermore, efficient computational frameworks capable of tracking complex nonlinear response branches and multistable solutions in such systems are still required.

Motivated by these challenges, the present work investigates the nonlinear dynamics of an electromagnetically controlled rotor system subjected to proportional-derivative feedback. An extended HQM framework combined with arc-length continuation is employed to compute nonlinear forced responses and track solution branches over a wide range of operating conditions. Particular attention is devoted to the characterization of periodic, quasiperiodic, and chaotic motions, the identification of routes to chaos, and the influence of control gains and electromagnetic coupling on the nonlinear response of the system.

2 System modeling of a flexible rotor supported by active magnetic bearings

2.1 System overview

The system investigated numerically is a flexible rotor supported by active magnetic bearings and rotating at the angular velocity ω, following the formulation proposed in [13], as illustrated in Figure 1.

For numerical modeling, the rotor is idealized as a lumped mass $2m_D$ concentrated at its mid-span, with two identical journal masses m_J located at the bearing stations. The corresponding schematic representation of the rotor-bearing system is shown in Figure 2.

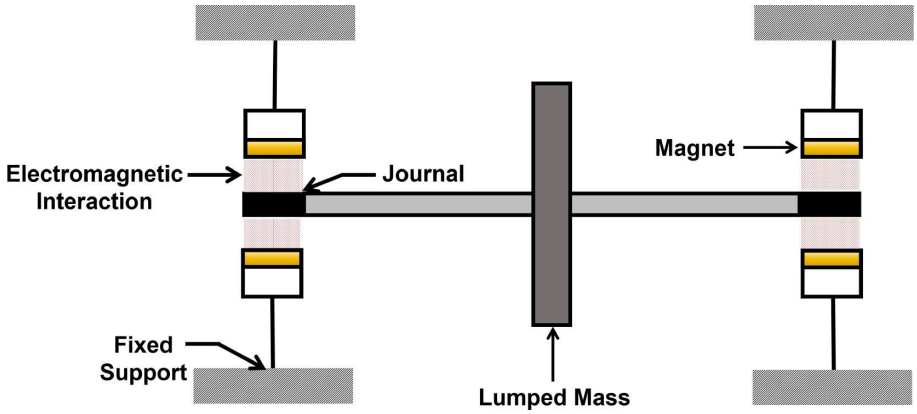

Fig. 1: Schematic of a flexible rotor supported by active magnetic bearings

To derive the governing equations of motion, several simplifying assumptions are introduced. The rotor is assumed to be symmetric, with its mass distributed between the mid-span and the bearing stations, and it rotates at a constant angular velocity ω. The rotor and support stiffnesses are considered radially symmetric, while the damping force acting on the mid-span disk due to air effects is modeled as viscous damping. Rotor imbalance is assumed to be confined to a single plane at the mid-span disk, axial motion is neglected, and gyroscopic effects are disregarded. Owing to the system symmetry, only one-half of the rotor-bearing configuration is considered in the

derivation. The system dynamics are therefore described by the lateral displacements (x_D, y_D) of the rotor mid-span center and (x_J, y_J) of the journal center.

The total kinetic energy K of the system includes contributions from translational motion and rotational inertia, is expressed as:

$$K = \frac{1}{2} m_D \left(\dot{x}_D^2 + \dot{y}_D^2 \right) + \frac{1}{2} m_J \left(\dot{x}_J^2 + \dot{y}_J^2 \right) + \frac{1}{2} I_{eq} \Omega^2 \tag{1}$$

The potential energy P includes contributions from shaft elasticity and gravitational loading, is given as:

$$P = \frac{1}{2} k_R \left((x_D - x_J)^2 + (y_D - y_J)^2 \right) + m_D g y_D + m_J g y_j \tag{2}$$

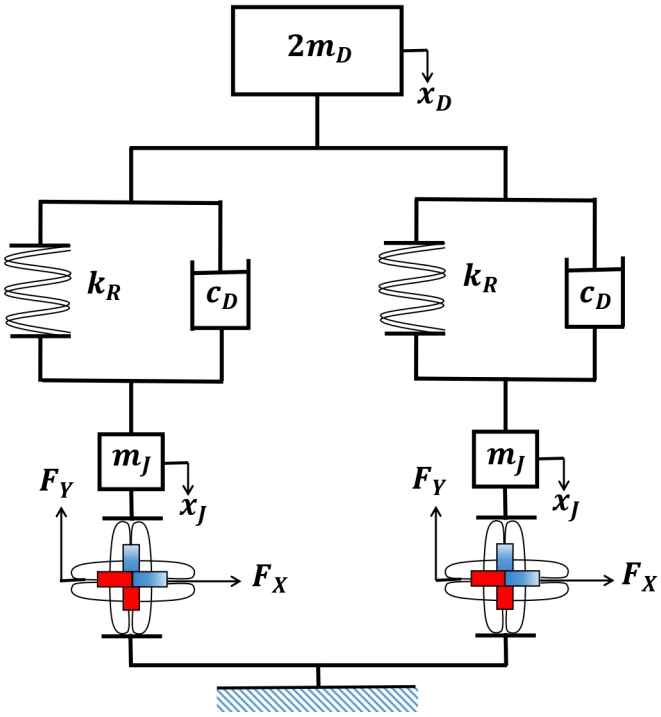

Fig. 2: Analytical model of the rotor-bearing system

The non-conservative forces are introduced through the generalized force components F_{x_D}, F_{y_D}, F_{x_J}, and F_{y_J}, which account for the imbalance excitation acting on the disk as well as the magnetic bearing control forces applied at the journal locations. These generalized forces are expressed as:

$$
\begin{aligned}
F_{x_D} &= 2m_D u\Omega^2 cos(\Omega t) \\
F_{y_D} &= 2m_D u\Omega^2 sin(\Omega t) \\
F_{x_J} &= F_x \\
F_{y_J} &= F_y
\end{aligned} \tag{3}
$$

Here, u denotes the eccentricity of the rotor center of mass, while F_x and F_y represent the magnetic bearing forces acting in the horizontal and vertical directions, respectively. The parameters k_R and c_D correspond to one-half of the shaft stiffness and viscous damping coefficient at the rotor mid-span.

By applying Lagrange's equations [2] to the generalized coordinates of the system, the governing equations of motion are obtained as follows:

$$
\begin{aligned}
m_D\ddot{x}_D &= -c_D\dot{x}_D - k_R\left(x_D - x_J\right) + m_D u\omega^2 cos(\omega t) \\
m_D\ddot{y}_D &= -c_D\dot{y}_D - k_R\left(y_D - y_J\right) - m_D g + m_D u\omega^2 sin(\omega t) \\
m_J\ddot{x}_J &= F_x - k_R\left(x_J - x_D\right) \\
m_J\ddot{y}_J &= F_y - k_R\left(y_J - y_D\right) - m_J g
\end{aligned} \tag{4}
$$

By dividing Eq.4 through by $m_D\omega_n^2 g_0$, the system of equations is given by:

$$
\begin{aligned}
\hat{x}_D^{''} &= -2\varsigma\frac{\omega r}{\omega_n}\hat{x}_D^{'} - \left(\frac{\omega_r}{\omega_n}\right)^2\left(\hat{x}_D - \hat{x}_J\right) + U\Omega^2 cos(\Omega\tau) \\
\hat{y}_D^{''} &= -2\varsigma\frac{\omega_r}{\omega_n}\hat{y}_D^{'} - \left(\frac{\omega_r}{\omega_n}\right)^2\left(\hat{y}_D - \hat{y}_J\right) - \left(\frac{\omega_r}{\omega_n}\right)^2 W + U\Omega^2 sin(\Omega\tau) \\
\hat{x}_J^{''} &= \frac{F_x}{m_J\omega_n^2 g_0} - \frac{1}{\gamma}\left(\frac{\omega_r}{\omega_n}\right)^2\left(\hat{x}_J - \hat{x}_D\right) \\
\hat{y}_J^{''} &= \frac{F_y}{m_J\omega_n^2 g_0} - \frac{1}{\gamma}\left(\frac{\omega_r}{\omega_n}\right)^2\left(\hat{y}_J - \hat{y}_D\right) - \left(\frac{\omega_r}{\omega_n}\right)^2 W
\end{aligned} \tag{5}
$$

The parameter ω_n denotes the linear natural frequency of the magnetic bearing system, while ω_r represents the pin-pin natural frequency of the flexible rotor, given by $\omega_r = \sqrt{\frac{k_R}{m_D}}$. The mass ratio γ is defined as the ratio of the journal mass m_J to the half-mass of the disc at the rotor mid-span m_D. The damping parameter ζ corresponds to half the viscous damping ratio acting on the disc at mid-span. The frequency ratio $\frac{\omega_n}{\omega_r}$ characterizes the relative stiffness of the magnetic bearing system compared to the flexible rotor. The gravity parameter W quantifies the unidirectional static misalignment force acting on both the rotor mid-span and the bearing stations. Rotor imbalance is captured by the unbalance parameter U, defined as the ratio of the eccentricity u of the rotor center of mass G from its geometric center of rotation, to the nominal air gap g_0 of the magnetic bearing. The speed parameter Ω is defined as

the ratio of the rotor operating speed ω to the magnetic bearing's natural frequency ω_n, and the non-dimensional time is denoted by τ.

Displacements, velocities, and accelerations of the rotor mid-span and journal in both the X- and Y-directions are non-dimensionalized with respect to the nominal air gap g_0.

The superscript $\hat{.}$ is used for non-dimensional degrees of freedom, $(\prime)$ and $(\prime\prime)$ denote the first and second derivatives of these variables with respect to τ, respectively.

2.2 Active Magnetic Forces

The forces generated by active magnetic bearings are derived from electromagnetic principles and the actuator geometry. In a typical radial magnetic bearing, the stator and rotor are constructed from laminated iron rings to minimize eddy current losses. Coils are wound around each stator pole, typically arranged in four quadrants. Opposing coils are excited in pairs to produce magnetic fields that attract the rotor toward the center, as shown in Figure 3. The magnetic flux generated by coil current flows through the stator, crosses the air gap, and enters the rotor, completing the magnetic circuit. The air gap is the dominant source of reluctance, and the magnetic force is proportional to the square of the magnetic flux and inversely proportional to the square of the air gap.

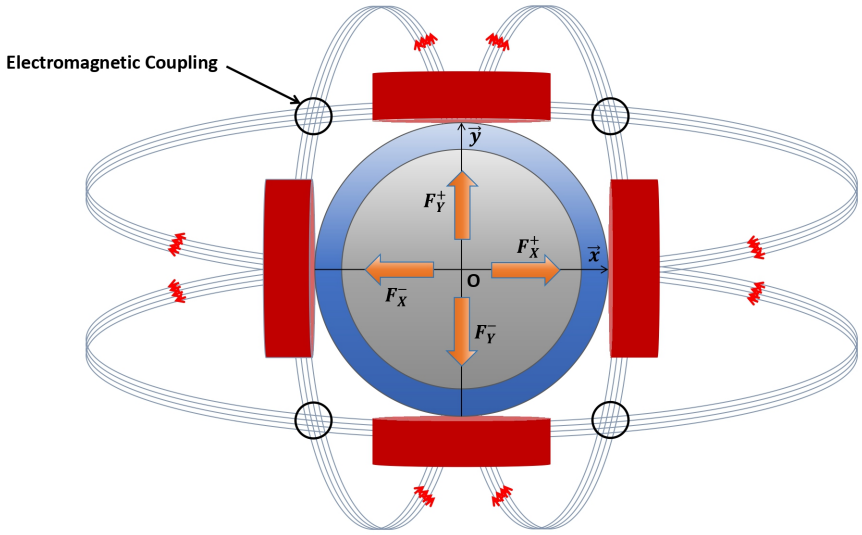

Fig. 3: Schematic of the active magnetic bearing configuration

Normalized magnetic forces $\frac{F_x}{m_J\Omega_n^2 g_0}$ and $\frac{F_y}{m_J\Omega_n^2 g_0}$ are given in [13] as follows:

$$\frac{F_x}{m_J\omega_n^2 g_0} = F_X^+ - F_X^- + \alpha x_J \left(F_Y^+ + F_Y^-\right)$$

$$\frac{F_y}{m_J\omega_n^2 g_0} = F_Y^+ - F_Y^- + \alpha y_J\left(F_X^+ + F_X^-\right) \tag{6}$$

where F_X^+ and F_X^- denote the magnetic forces in X^+ and X^- directions, respectively, and F_Y^+ and F_Y^- denote the magnetic forces in Y^+ and Y^- directions, respectively.

$$F_X^+ = \frac{1}{4\left(P-1\right)}\left[\frac{\left(1-Px_j-Dx_J^{'}\right)^2}{\left(1-x_j\right)^2}\right] \quad F_Y^+ = \frac{1}{4\left(P-1\right)}\left[\frac{\left(1-Py_j-Dy_J^{'}\right)^2}{\left(1-y_j\right)^2}\right]$$
$$F_X^- = \frac{1}{4\left(P-1\right)}\left[\frac{\left(1+Px_j+Dx_J^{'}\right)^2}{\left(1+x_j\right)^2}\right] \quad F_Y^- = \frac{1}{4\left(P-1\right)}\left[\frac{\left(1+Py_j+Dy_J^{'}\right)^2}{\left(1+y_j\right)^2}\right] \tag{7}$$

P, D and α are respectively the non-dimensional proportional and derivative feedback gains of the controller and the geometric coupling parameter. The system parameters are summarized in Table 1.

Table 1: System parameters

System parameters	ζ	$\frac{\omega_n}{\omega_r}$	U	γ	W	P	D	α
Values	0.001	1.5	0.1	0.2	0.025	1.1	0.03	0.28

3 Application of the Embedded HQM-Arc Length Continuation

3.1 Method Formulation

The Harmonic Quadrature Method (HQM) belongs to the broader family of differential quadrature methods (DQM), which aim to achieve highly accurate interpolation of function derivatives over a given mesh. Unlike conventional DQM approaches that rely on polynomial bases, HQM employs harmonic bases, making it particularly effective for modeling periodic phenomena. In this work, HQM is implemented to compute the steady-state periodic solution of the nonlinear differential system governing the rotor dynamics.

The time scale discretization τ_i is defined as:

$$\tau_i = \frac{i}{n_\tau}, 0 \leq \tau_i < 1, 0 \leq i < n_\tau \tag{8}$$

where n_τ is the number of time increments. For HQM, this number must be an odd integer to ensure proper harmonic representation.

The initial conditions are reformulated to reflect periodicity in the time domain:

$$\begin{aligned} \{\hat{x}\}_{\tau=0} &= \{\hat{x}\}_{\tau=1} \\ \left\{\hat{x'}\right\}_{\tau=0} &= \left\{\hat{x'}\right\}_{\tau=1} \end{aligned} \tag{9}$$

To discretize the equations of motion in the time domain, the first- and second-order time derivatives are replaced by the HQM derivative matrices $[D_\tau]_1^*$ and $[D_\tau]_2^*$. Time-dependent variables are represented using diagonal matrices, leading to the following discretized form of the system's equation of motion:

$$\left([D_\tau]_2^* [M] + [D_\tau]_1^* [C] + [I]^* [K]\right) \{\hat{x}\} = \left\{\hat{F}\right\} \tag{10}$$

where $[D_\tau]_1^*$,$[D_\tau]_2^*$,$[I]^*$, $[M]$, $[C]$, $[K]$, $[Z]$, $\{\hat{x}\}$ and $\left\{\hat{F}\right\}$ are given by :

$$[D_\tau]_1^* = \begin{bmatrix} [D_\tau]_{1_{n_\tau \times n_\tau}} & [Z]_{n_\tau \times n_\tau} & [Z]_{n_\tau \times n_\tau} & [Z]_{n_\tau \times n_\tau} \\ [Z]_{n_\tau \times n_\tau} & [D_\tau]_{1_{n_\tau \times n_\tau}} & [Z]_{n_\tau \times n_\tau} & [Z]_{n_\tau \times n_\tau} \\ [Z]_{n_\tau \times n_\tau} & [Z]_{n_\tau \times n_\tau} & [D_\tau]_{1_{n_\tau \times n_\tau}} & [Z]_{n_\tau \times n_\tau} \\ [Z]_{n_\tau \times n_\tau} & [Z]_{n_\tau \times n_\tau} & [Z]_{n_\tau \times n_\tau} & [D_\tau]_{1_{n_\tau \times n_\tau}} \end{bmatrix} \tag{11}$$

$$[D_\tau]_2^* = \begin{bmatrix} [D_\tau]_{2_{n_\tau \times n_\tau}} & [Z]_{n_\tau \times n_\tau} & [Z]_{n_\tau \times n_\tau} & [Z]_{n_\tau \times n_\tau} \\ [Z]_{n_\tau \times n_\tau} & [D_\tau]_{2_{n_\tau \times n_\tau}} & [Z]_{n_\tau \times n_\tau} & [Z]_{n_\tau \times n_\tau} \\ [Z]_{n_\tau \times n_\tau} & [Z]_{n_\tau \times n_\tau} & [D_\tau]_{2_{n_\tau \times n_\tau}} & [Z]_{n_\tau \times n_\tau} \\ [Z]_{n_\tau \times n_\tau} & [Z]_{n_\tau \times n_\tau} & [Z]_{n_\tau \times n_\tau} & [D_\tau]_{2_{n_\tau \times n_\tau}} \end{bmatrix} \tag{12}$$

$$[I]^* = \begin{bmatrix} [I]_{n_\tau \times n_\tau} & [Z]_{n_\tau \times n_\tau} & [Z]_{n_\tau \times n_\tau} & [Z]_{n_\tau \times n_\tau} \\ [Z]_{n_\tau \times n_\tau} & [I]_{n_\tau \times n_\tau} & [Z]_{n_\tau \times n_\tau} & [Z]_{n_\tau \times n_\tau} \\ [Z]_{n_\tau \times n_\tau} & [Z]_{n_\tau \times n_\tau} & [I]_{n_\tau \times n_\tau} & [Z]_{n_\tau \times n_\tau} \\ [Z]_{n_\tau \times n_\tau} & [Z]_{n_\tau \times n_\tau} & [Z]_{n_\tau \times n_\tau} & [I]_{n_\tau \times n_\tau} \end{bmatrix} \tag{13}$$

$$[M] = \begin{bmatrix} [I]_{n_\tau \times n_\tau} & [Z]_{n_\tau \times n_\tau} & [Z]_{n_\tau \times n_\tau} & [Z]_{n_\tau \times n_\tau} \\ [Z]_{n_\tau \times n_\tau} & [I]_{n_\tau \times n_\tau} & [Z]_{n_\tau \times n_\tau} & [Z]_{n_\tau \times n_\tau} \\ [Z]_{n_\tau \times n_\tau} & [Z]_{n_\tau \times n_\tau} & [I]_{n_\tau \times n_\tau} & [Z]_{n_\tau \times n_\tau} \\ [Z]_{n_\tau \times n_\tau} & [Z]_{n_\tau \times n_\tau} & [Z]_{n_\tau \times n_\tau} & [I]_{n_\tau \times n_\tau} \end{bmatrix} \tag{14}$$

$$[C] = \begin{bmatrix} 2\varsigma \frac{\omega_r}{\omega_n} [D_\tau]_1 & [Z]_{n_\tau \times n_\tau} & [Z]_{n_\tau \times n_\tau} & [Z]_{n_\tau \times n_\tau} \\ [Z]_{n_\tau \times n_\tau} & 2\varsigma \frac{\omega_r}{\omega_n} [D_\tau]_1 & [Z]_{n_\tau \times n_\tau} & [Z]_{n_\tau \times n_\tau} \\ [Z]_{n_\tau \times n_\tau} & [Z]_{n_\tau \times n_\tau} & [Z]_{n_\tau \times n_\tau} & [Z]_{n_\tau \times n_\tau} \\ [Z]_{n_\tau \times n_\tau} & [Z]_{n_\tau \times n_\tau} & [Z]_{n_\tau \times n_\tau} & [Z]_{n_\tau \times n_\tau} \end{bmatrix} \tag{15}$$

$$[K] = \begin{bmatrix} \left(\frac{\omega_r}{\omega_n}\right)^2 [I]_{n_\tau \times n_\tau} & [Z]_{n_\tau \times n_\tau} & -\left(\frac{\omega_r}{\omega_n}\right)^2 [I]_{n_\tau \times n_\tau} & [Z]_{n_\tau \times n_\tau} \\ [Z]_{n_\tau \times n_\tau} & \left(\frac{\omega_r}{\omega_n}\right)^2 [I]_{n_\tau \times n_\tau} & [Z]_{n_\tau \times n_\tau} & -\left(\frac{\omega_r}{\omega_n}\right)^2 [I]_{n_\tau \times n_\tau} \\ -\frac{1}{\gamma}\left(\frac{\omega_r}{\omega_n}\right)^2 [I]_{n_\tau \times n_\tau} & [Z]_{n_\tau \times n_\tau} & \frac{1}{\gamma}\left(\frac{\omega_r}{\omega_n}\right)^2 [I]_{n_\tau \times n_\tau} & [Z]_{n_\tau \times n_\tau} \\ [Z]_{n_\tau \times n_\tau} & -\frac{1}{\gamma}\left(\frac{\omega_r}{\omega_n}\right)^2 [I]_{n_\tau \times n_\tau} & [Z]_{n_\tau \times n_\tau} & \frac{1}{\gamma}\left(\frac{\omega_r}{\omega_n}\right)^2 [I]_{n_\tau \times n_\tau} \end{bmatrix} \tag{16}$$

$$[Z] = \begin{bmatrix} 0 & \cdots & 0 \\ \vdots & \ddots & \vdots \\ 0 & \cdots & 0 \end{bmatrix} \tag{17}$$

$$\{\hat{x}\} = \begin{Bmatrix} \{\hat{x}_D\} \\ \{\hat{y}_D\} \\ \{\hat{x}_J\} \\ \{\hat{y}_J\} \end{Bmatrix} = \begin{Bmatrix} \hat{x}_D(\tau_0) \\ \vdots \\ \hat{x}_D(\tau_{n_\tau-1}) \\ --- \\ \hat{y}_D(\tau_0) \\ \vdots \\ \hat{y}_D(\tau_{n_\tau-1}) \\ --- \\ \hat{x}_J(\tau_0) \\ \vdots \\ \hat{x}_J(\tau_{n_\tau-1}) \\ --- \\ \hat{y}_J(\tau_0) \\ \vdots \\ \hat{y}_J(\tau_{n_\tau-1}) \end{Bmatrix} \left\{\hat{F}\right\} = \begin{Bmatrix} U\Omega^2 cos(\Omega\tau_0) \\ \vdots \\ U\Omega^2 cos(\Omega\tau_{n_\tau-1}) \\ ---------- \\ U\Omega^2 sin(\Omega\tau_0) - \left(\frac{\omega_r}{\omega_n}\right)^2 W \\ \vdots \\ U\Omega^2 sin(\Omega\tau_{n_\tau-1}) - \left(\frac{\omega_r}{\omega_n}\right)^2 W \\ ---------- \\ \frac{F_x(\tau_0)}{m_J\omega_n^2 g_0} \\ \vdots \\ \frac{F_x(\tau_{n_\tau-1})}{m_J\omega_n^2 g_0} \\ ---------- \\ \frac{F_y(\tau_0)}{m_J\omega_n^2 g_0} - \left(\frac{\omega_r}{\omega_n}\right)^2 W \\ \vdots \\ \frac{F_y(\tau_{n_\tau-1})}{m_J\omega_n^2 g_0} - \left(\frac{\omega_r}{\omega_n}\right)^2 W \end{Bmatrix} \tag{18}$$

Here, $[I]_{n_\tau \times n_\tau}$ and $[Z]_{n_\tau \times n_\tau}$ denote, respectively, the identity matrix and the null matrix of dimension $n_\tau \times n_\tau$.

The first and second time derivative are substituted by the HQM first and second derivative matrices $[D_\tau]_1$ and $[D_\tau]_2$, constructed using harmonic interpolation theory as mentioned in [1, 2] and expressed as:

$$[D_\tau]_m = (2\pi)^m H_\tau^{(m)}, m = 1, 2 \tag{19}$$

where

$$\left[H_\tau^{(m)}\right]_{i,j} = \begin{cases} \frac{\prod_{S\tau_i}}{2[\Delta_{S\tau}]_{i,j}\prod_{S\tau_j}} & m=1, i\neq j \\ \left[H_\tau^{(1)}\right]_{i,j}\left(2\left[H_\tau^{(1)}\right]_{i,i} - [\Delta_{C\tau}]_{i,j}\right) & m=2, i\neq j \\ -\sum_{k=1,k\neq i}\left[H_\tau^{(m)}\right]_{i,k} & m>0; i=j \end{cases} \tag{20}$$

The terms $[\Delta_{S\tau}]_{i,j}$, $[\Delta_{C\tau}]_{i,j}$ and $\prod S\tau_i$ are expressed as:

$$\begin{cases} [\Delta_{S\tau}]_{i,j} = sin\left(\frac{\tau_i-\tau_j}{2}\right) & 1\leq i,j\leq n_\tau \\ [\Delta_{C\tau}]_{i,j} = cot\left(\frac{\tau_i-\tau_j}{2}\right) & 1\leq i,j\leq n_\tau \\ \prod S\tau_i = \prod_{k=1,k\neq i}[\Delta_{S\tau}]_{i,k} & 1\leq i\leq n_\tau \end{cases} \tag{21}$$

The final solution is assessed by computing the residual vector $\{R\}$ and verifying that it satisfies the convergence criterion $\left\|R\right\| < \varepsilon = 10^{-8}$:

$$\{R\} = \left([D_\tau]_2^*[M] + [D_\tau]_1^*[C] + [I]^*[K]\right)\{\hat{x}\} - \left\{\hat{F}\right\} \tag{22}$$

Upon convergence, the time response is evaluated by computing the Fourier coefficient matrix T given by:

$$[T] = \begin{bmatrix} 1 & cos(\Omega\tau_0) & sin(\Omega\tau_0) & \cdots & cos(H\Omega\tau_0) & sin(H\Omega\tau_0) \\ \vdots & \vdots & \vdots & \vdots & \vdots & \vdots \\ 1 & cos(\Omega\tau_{n_\tau-1}) & sin(\Omega\tau_{n_\tau-1}) & \cdots & cos(H\Omega\tau_{n_\tau-1}) & sin(H\Omega\tau_{n_\tau-1}) \end{bmatrix}_{n_\tau\times n_\tau} \tag{23}$$

The response is then represented in terms of the Fourier coefficients $\{\bar{x}\}$ as follows:

$$\{\bar{x}\} = [[T]]\{\hat{x}\} \tag{24}$$

where the matrix $[[T]]$ is given by:

$$[[T]] = \begin{bmatrix} [T] & [Z]_{n_\tau\times n_\tau} & [Z]_{n_\tau\times n_\tau} & [Z]_{n_\tau\times n_\tau} \\ [Z]_{n_\tau\times n_\tau} & [T] & [Z]_{n_\tau\times n_\tau} & [Z]_{n_\tau\times n_\tau} \\ [Z]_{n_\tau\times n_\tau} & [Z]_{n_\tau\times n_\tau} & [T] & [Z]_{n_\tau\times n_\tau} \\ [Z]_{n_\tau\times n_\tau} & [Z]_{n_\tau\times n_\tau} & [Z]_{n_\tau\times n_\tau} & [T] \end{bmatrix}_{4n_\tau\times 4n_\tau} \tag{25}$$

The proposed HQM-Arc Length Continuation framework combines the Harmonic Quadrature Method with a predictor–corrector continuation strategy to efficiently trace nonlinear response branches. Following the HQM discretization of the governing equations, the nonlinear periodic response is represented by a set of algebraic equations whose solution depends on a continuation parameter, such as the excitation frequency or rotational speed. Starting from a converged equilibrium point, a predictor step (HQM_P) is first performed by advancing a prescribed arc-length increment along the tangent direction of the solution branch. This predicted state provides an initial estimate of the subsequent equilibrium point. Since the predictor generally does not satisfy the nonlinear governing equations exactly, a correction stage (HQM_C) is subsequently carried out. During this stage, the HQM equations and the arc-length

constraint are solved simultaneously through an iterative procedure until convergence is achieved.

Let the HQM discretization lead to the nonlinear algebraic system:

$$R(X, P) = 0 \tag{26}$$

where X is the vector containing the harmonic coefficients and P is the continuation parameter.

Let $\overline{HQM}_c^i$, $\overline{HQM}_p^{i+1}$ and $\overline{HQM}_c^{i+1}$ be respectively the corrected solution at step i, the predicted solution at step $i+1$, and the corrected solution at step $i+1$ obtained by the HQM:

$$\overline{HQM}_c^i = \begin{Bmatrix} X_c^i \\ P_c^i \end{Bmatrix} \qquad \overline{HQM}_p^{i+1} = \begin{Bmatrix} X_p^{i+1} \\ P_p^{i+1} \end{Bmatrix} \qquad \overline{HQM}_c^{i+1} = \begin{Bmatrix} X_c^{i+1} \\ P_c^{i+1} \end{Bmatrix} \tag{27}$$

And indices r, f correspond respectively to the first and second composant of the vector $\overline{HQM}$.

A known converged solution point $\overline{HQM}_c^i$, the predictor solution $\overline{HQM}_p^{i+1}$, is obtained by moving along the tangent vector T_i

$$\overline{HQM}_p^{i+1} = \overline{HQM}_c^i + \Delta s T_i \tag{28}$$

Where Δs denotes the prescribed arc-length step.

The predicted point generally does not satisfy the nonlinear equations exactly. Therefore, a correction stage $\overline{HQM}_c^{i+1}$ is performed by solving:

$$R(\overline{HQM}_c^{i+1}) = 0 \tag{29}$$

subject to the arc-length constraint:

$$\begin{aligned} (\Delta s)^2 \;=\; & \left(\overline{HQM}_c^{i+1}(r) - \overline{HQM}_c^i(r)\right)^T \left(\overline{HQM}_c^{i+1}(r) - \overline{HQM}_c^i(r)\right) \\ & +\; \psi \left(\overline{HQM}_c^{i+1}(f) - \overline{HQM}_c^i(f)\right)^2 \end{aligned} \tag{30}$$

where ψ is a scaling factor introduced to balance the contributions of the response variables and the continuation parameter.

The corresponding augmented system solved during the correction stage is:

$$\begin{bmatrix} R(\overline{HQM}_c^{i+1}) \\ g\left(R(\overline{HQM}_c^{i+1})\right) \end{bmatrix} = 0 \tag{31}$$

Where $g(R(\overline{HQM}_c^{i+1})$ is given as :

$$\begin{aligned} g(R(\overline{HQM}_c^{i+1}) \;=\; & \left(\overline{HQM}_c^{i+1}(r) - \overline{HQM}_c^i(r)\right)^T \left(\overline{HQM}_c^{i+1}(r) - \overline{HQM}_c^i(r)\right) \\ & +\; \psi \left(\overline{HQM}_c^{i+1}(f) - \overline{HQM}_c^i(f)\right)^2 - (\Delta s)^2 \end{aligned}$$

The arc-length condition controls the combined variation of the response vector X and the continuation parameter P, thereby maintaining a nearly constant progression along the equilibrium path. As a result, the continuation process remains robust in the vicinity of turning points, fold bifurcations, and strongly nonlinear regions, where conventional incremental techniques often fail. The corrected solution obtained at the end of each iteration $\overline{HQM}_c^i$ serves as the starting point for the next predictor step $\overline{HQM}_p^{i+1}$, allowing the complete nonlinear branch to be followed continuously, as illustrated in Figure 4. Repetition of the predictor-corrector sequence enables the accurate tracking of stable and unstable solution branches and provides a comprehensive characterization of the nonlinear dynamic behavior of the rotor system.

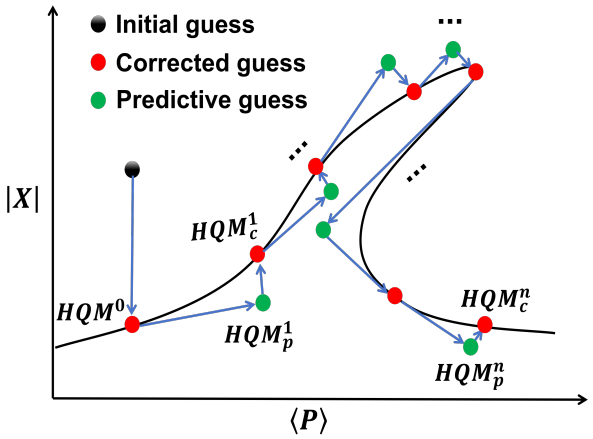

Fig. 4: Predictor-corrector arc-length continuation scheme

3.2 Method Validation

To verify the robustness of the HQM-arc-length continuation, three benchmark cases covering different nonlinearity types (magnetic, hydrodynamic, cubic) are considered. The first validation is against the work of Chinta and Palazzolo [18], where the system is a magnetic rotor bearing and the equations of motion describing the journal displacement are presented in Eq.32 as follows:

$$\begin{aligned} x'' &= f_e - f_l + \alpha\,(f_t + f_b) + E\Omega^2 cos\,(\Omega\tau) \\ y'' &= f_t - f_b + \alpha\,(f_e + f_l) + E\Omega^2 sin\,(\Omega\tau) - G \end{aligned} \tag{32}$$

where x and y denote respectively the displacements of journal in X- and Y-axes, E is the eccentricity and G is the rotor weight. As shown in Figure 6, the Runge-Kutta scheme and the TCM in both increasing and decreasing frequency sweeps failed to detect the nonlinear branches. In contrast, Figure 5 demonstrates that the

HQM-arc-length continuation method successfully captured all nonlinear branches. Furthermore, the convergence study presented in Figure 5 shows that a minimum of $H = 11$ harmonics is required to achieve a convergent solution for the hydrodynamic bearing validation case.

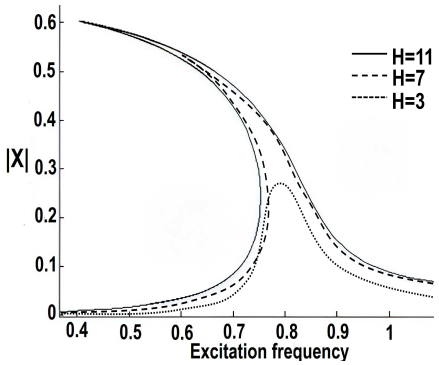

Fig. 5: Nonlinear frequency response of the magnetic bearing rotor system obtained using HQM

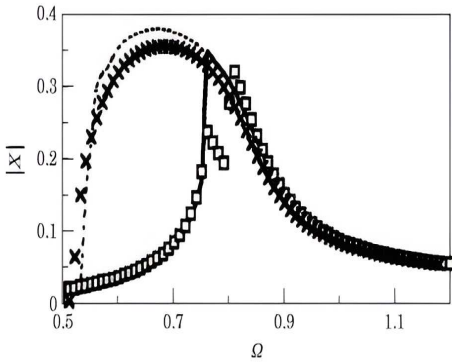

Fig. 6: Nonlinear frequency response of the magnetic bearing rotor system obtained using TCM and RK from [18]

The HQM method is then validated against the work of Inayat-Hussain [25] as shown in Figure 8. In this context, a rotor supported by a hydrodynamic bearing model is described through two equations of motion:

$$
\begin{aligned}
x'' &= -B\left[\frac{x}{\varepsilon}\left(I_1\varepsilon' + I_2\varepsilon\varphi'\right) - \frac{y}{\varepsilon}\left(I_2\varepsilon' + I_3\varepsilon\varphi'\right)\right] - S^2x + Ucos(\tau) \\
y'' &= -B\left[\frac{y}{\varepsilon}\left(I_1\varepsilon' + I_2\varepsilon\varphi'\right) + \frac{y}{\varepsilon}\left(I_2\varepsilon' + I_3\varepsilon\varphi'\right)\right] - S^2y + Usin(\tau) - W
\end{aligned}
\tag{33}
$$

In this formulation, x and y denote the non-dimensional displacements of the rotor's geometric center along the X- and Y-axes, respectively. The parameters of the governing equations are detailed in [25]. A convergence study was conducted to determine the appropriate number of harmonics, H. Figure 7 presents the frequency response curves (FRCs) for various values of H. The curves begin to overlap once the number of harmonics exceeds 11, indicating that a minimum of nine harmonics is required to achieve a convergent solution.

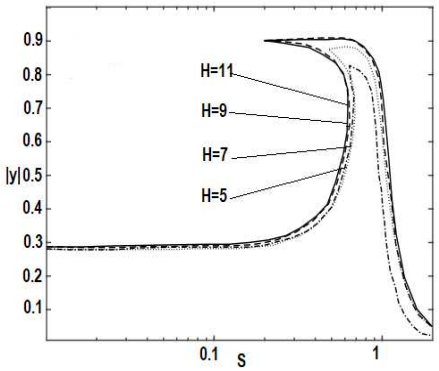

Fig. 7: Nonlinear frequency response of the hydrodynamic bearing rotor system obtained using HQM

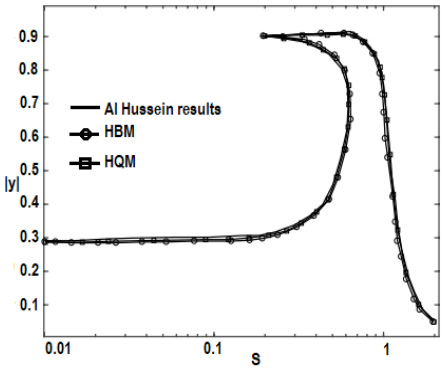

Fig. 8: Nonlinear frequency response of the hydrodynamic bearing rotor system obtained using RK from [25]

The subsequent validation is performed against the results of Min Sun and Jianen Chen [26], where an energy sink is modeled through two equations of motion:

$$\ddot{w} + \gamma_1 \dot{w} + Kw + k_1 w^3 + k_2 (w - v)^3 + \gamma_2 (\dot{w} - \dot{v}) = f cos(\Omega t)$$
$$\varepsilon \ddot{v} + k_2 (v - w)^3 + \gamma_2 (\dot{v} - \dot{w}) = 0$$

In this case, the HQM method is coupled with the arc-length continuation algorithm, using seven harmonics. Unlike Min Sun results [26] presented in Figure 9, the nonlinear branch is successfully captured as shown in Figure 10

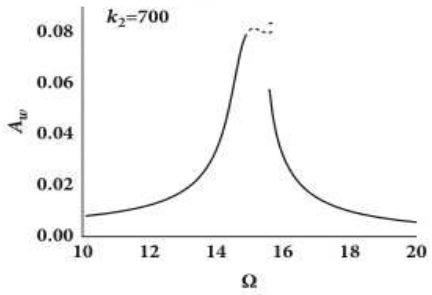

Fig. 9: Nonlinear frequency response of the Energy Sink system using the analytical method from [26]

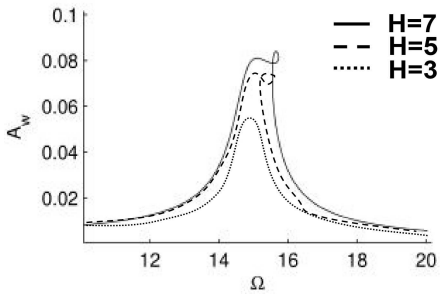

Fig. 10: Nonlinear frequency response of the Energy Sink system using HQM

Based on the convergence studies conducted throughout the validation cases, $H = 11$ harmonics is adopted for all subsequent computations, as this value guarantees a fully converged solution while maintaining computational efficiency.

4 Numerical Results

4.1 Periodicity Analysis

The numerical bifurcation analysis was performed by sampling the rotor response at stroboscopic points $y_j(nT)$ while sweeping the excitation frequency ω in both directions. Although the overall structure of the bifurcation diagrams was similar, small but significant differences were observed between the forward (Figure 11) and the backward direction (Figure 12). In particular, at certain values of ω, the amplitude of oscillation and the number of coexisting periodic branches differed between the two cases. These discrepancies indicate the presence of hysteresis and multistability, where the system's response depends not only on the current excitation frequency but also on the path taken through parameter space.

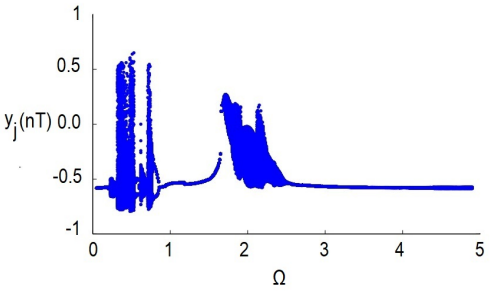

Fig. 11: Bifurcation diagram with increasing frequency Ω

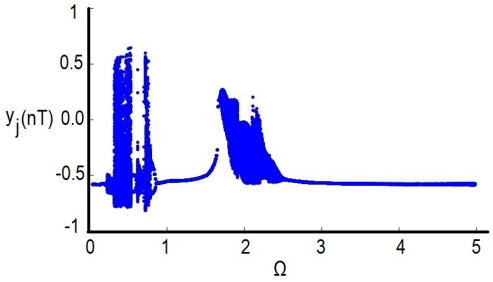

Fig. 12: Bifurcation diagram with decreasing frequency Ω

Several distinct regions of the bifurcation diagram were identified in Figures 13, 14, 15, 16, and 17. For each region, a representative value of the normalized rotational speed Ω was selected to analyze the corresponding dynamical behavior in detail. This approach allows the systematic characterization of periodic, multi-periodic, quasi-periodic, and chaotic regimes, each confirmed by complementary diagnostics including FFT spectra, phase portraits, and Poincare maps.

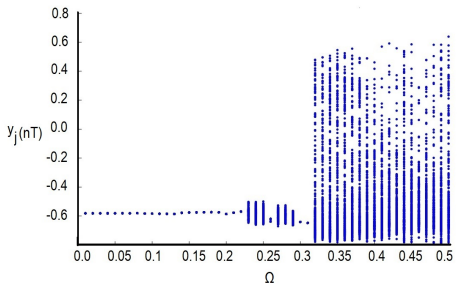

Fig. 13: Bifurcation diagram for Ω in [0;0.5]

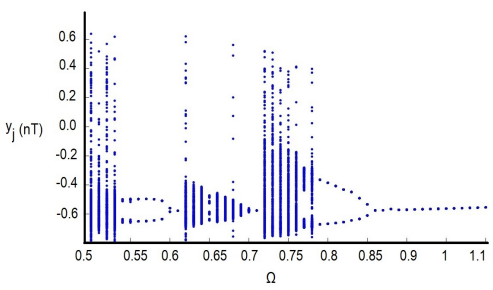

Fig. 14: Bifurcation diagram for Ω in [0.5;1]

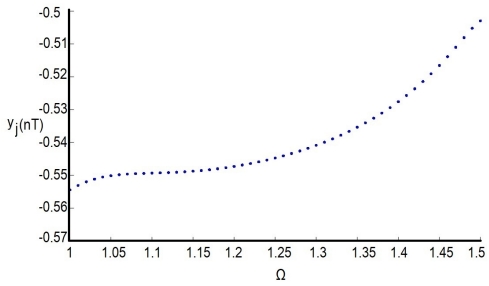

Fig. 15: Bifurcation diagram for Ω in [1;1.5]

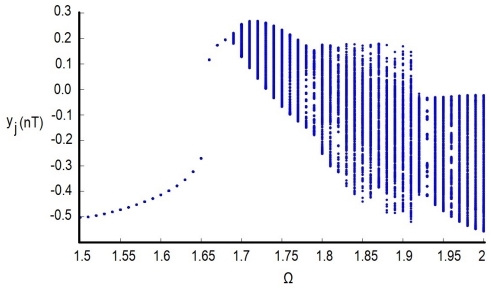

Fig. 16: Bifurcation diagram for Ω in [1.5;2]

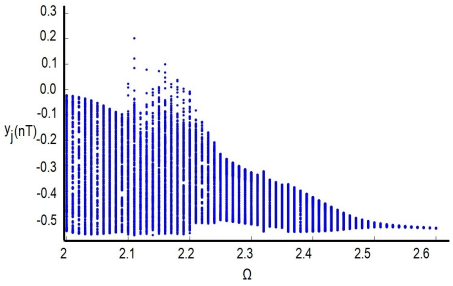

Fig. 17: Bifurcation diagram for Ω in [2;2.6]

For multiple disjoint parameter intervals, namely $\Omega \in [0, 0.22]$, $[0.30, 0.32]$, $\{0.61\}$, $[0.86, 1.68]$, and $[2.5, 5]$, the system exhibits a periodic response. A representative case is selected at $\Omega = 1.2$. As illustrated in Figure 18, the frequency spectrum shows a

single dominant peak at $X_r = 0.191$, indicating a purely periodic motion. The phase portrait collapses into a single closed orbit, while the Poincaré section reduces to a single fixed point (Figure 19), characteristic of a limit-cycle response across all periodic windows.

For $\Omega \in \{0.26\}, [0.54, 0.60], [0.78, 0.85]$, a period-2 response is observed, indicating a period-doubling regime. At $\Omega = 0.84$, as shown in Figure 20, the Fourier spectrum shows a dominant component $X_r = 0.133$ together with a subharmonic at $X_r/2$, consistent with the period-doubled nature of the oscillation. The phase portrait consists of two closed orbits, while the Poincaré section reduces to two discrete points (Figure 21).

A higher-order periodic regime is observed at $\Omega = 0.65$, corresponding to a period-7 response. The frequency spectrum is dominated by the fundamental component $X_r = 0.103$, together with additional harmonic contributions associated with the multi-cycle response, as illustrated in Figure 22. The phase portrait exhibits seven distinct closed orbits, and the Poincaré map contains seven isolated points (Figure 23), in agreement with a period-7 motion.

For $\Omega \in [0.66, 0.71]$, the system exhibits quasi-periodic behavior characterized by the interaction of two incommensurate frequencies. At $\Omega = 0.68$, the spectrum shows a fundamental component $X_r = 0.108$ together with modulation frequencies generating sidebands at $X_r \pm X_m$, as presented in Figure 24. The phase portrait evolves on an invariant torus, while the Poincaré section forms closed invariant curves (Figure 25), signatures of quasi-periodic motion.

For $\Omega \in [1.69, 1.80], [1.80, 1.82], [2.4, 2.5]$, the system exhibits a second quasi-periodic regime with multiple interacting frequencies. At $\Omega = 1.81$, the Fourier spectrum shows a dominant component $X_r = 0.288$ accompanied by additional modulation frequencies, generating multiple sidebands as shown in Figure 26. The phase portrait evolves on a distorted invariant torus, and the Poincaré section forms closed invariant double curves (Figure 27), indicative of multi-frequency quasi-periodicity.

Finally, chaotic behavior is observed for $\Omega \in [0.22, 0.29] \cup (0.32, 0.54) \cup [0.62, 0.64] \cup [0.72, 0.78] \cup [1.82, 2.4]$. As illustrated in Figure 28, at $\Omega = 2.15$, the Fourier spectrum exhibits a broadband distribution with no dominant periodic structure. The Poincaré section becomes a scattered set of points, while the phase portrait forms a strange attractor (Figure 29), hallmarks of chaotic dynamics.

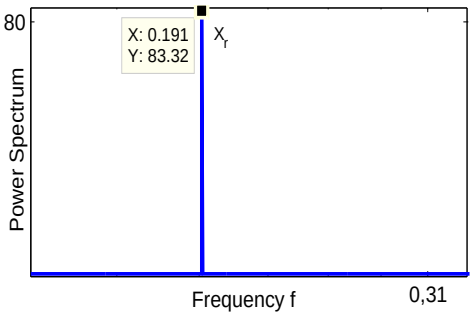

Fig. 18: FFT curve for Ω=1.2

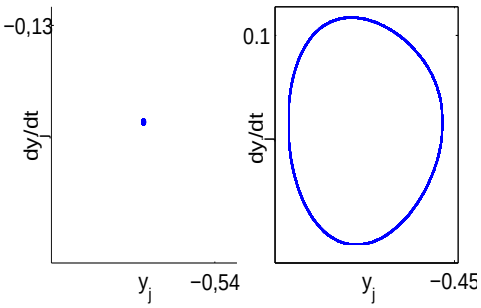

Fig. 19: Phase portrait and Poincare Map for Ω=1.2

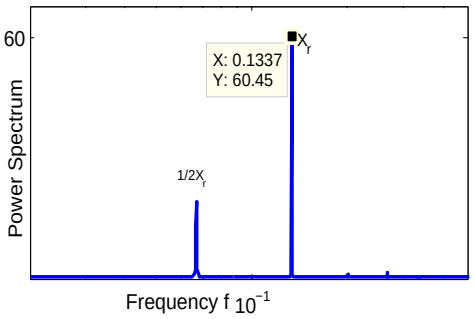

Fig. 20: FFT curve for Ω=0.84

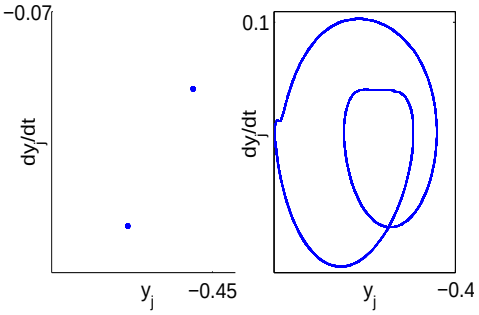

Fig. 21: Phase portrait and Poincare Map for Ω=0.84

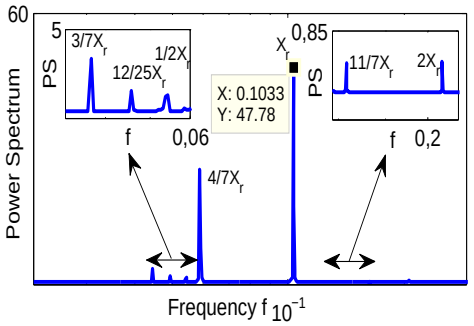

Fig. 22: FFT curve for Ω=0.65

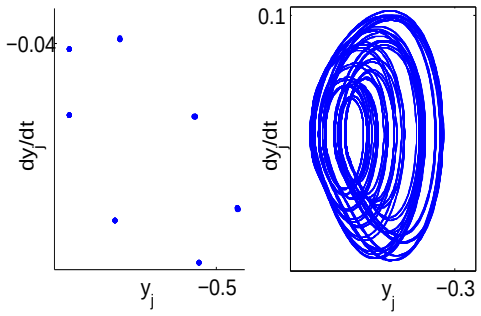

Fig. 23: Phase portrait and Poincare Map for Ω=0.65

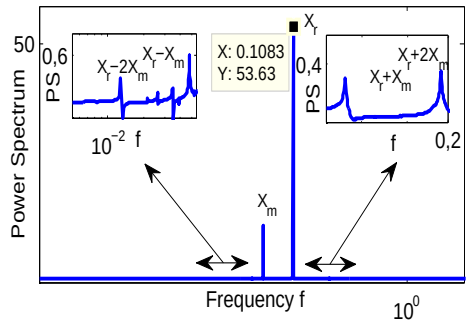

Fig. 24: FFT curve for Ω=0.68

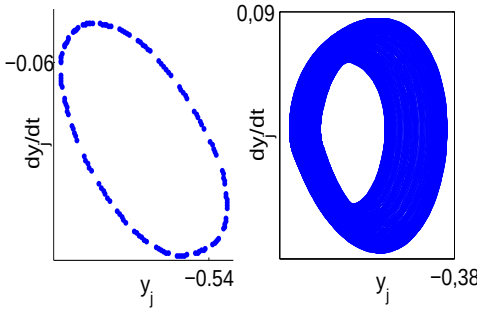

Fig. 25: Phase portrait and Poincare Map for Ω=0.68

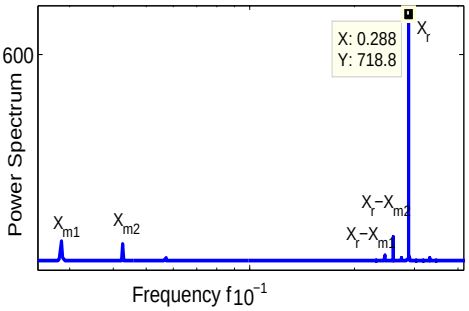

Fig. 26: FFT curve for Ω=1.81

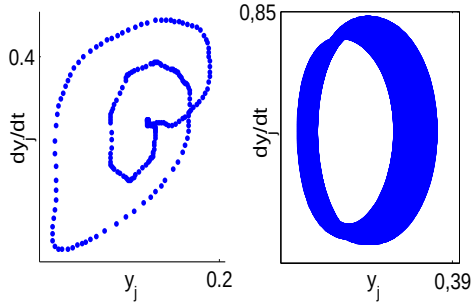

Fig. 27: Phase portrait and Poincare Map for Ω=1.81

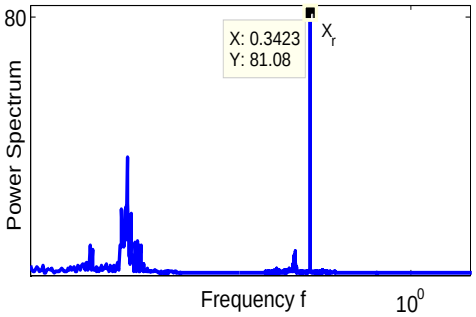

Fig. 28: FFT curve for Ω=2.15

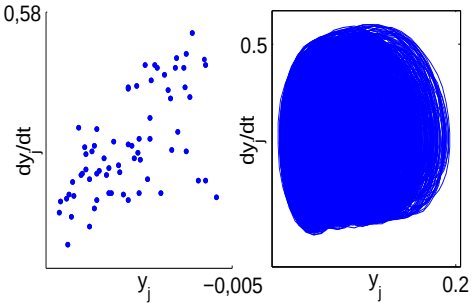

Fig. 29: Phase portrait and Poincare Map for Ω=2.15

4.2 Investigation of Routes to Chaos

The routes to chaos are discussed by considering representative transitions.

In the first stage, the system exhibits windows of chaos embedded between periodic and chaotic regimes, as illustrated in Figure 30. The bifurcation diagram evolves from discrete points to continuous lines, indicating the onset of irregular behavior. The corresponding time response shows that at $\Omega = 0.22657$ the motion remains one-periodic, whereas at $\Omega = 0.2268$ the response becomes chaotic.

In the next stage, the chaotic motion terminates through windows leading to a two-periodic response, as shown in Figure 31. The bifurcation diagram illustrates this transition clearly, where at $\Omega = 0.5386$ the temporal response is chaotic, whereas at $\Omega = 0.5388$ the motion stabilizes into a two-periodic regime.

Further transitions are observed in the bifurcation diagram, where additional windows open to transform the response from one-periodic to chaotic. At $\Omega = 0.6105$ the response is one-periodic, while at $\Omega = 0.611$ it becomes chaotic, as shown in Figure 32. The system then routes back to one-periodic motion around $\Omega = 0.714$, where the chaotic stage is closed by windows. At $\Omega = 0.713$ the response is chaotic, while at $\Omega = 0.714$ it stabilizes into one-periodic motion, as revealed in Figure 33.

A return to chaos is again observed at $\Omega = 0.715$, followed by a transition to a bi-periodic regime through period-halving. For instance, at $\Omega = 0.78$ the response remains chaotic, whereas at $\Omega = 0.781$ the motion stabilizes into bi-periodic behavior, as conveyed in Figure 34.

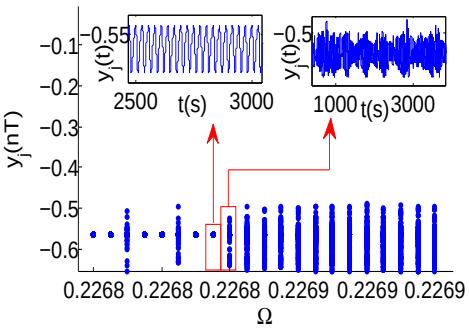

Fig. 30: Transition from a periodic to a chaotic motion near $\Omega = 0.2266$

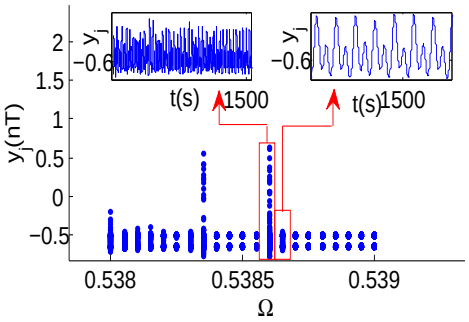

Fig. 31: Chaos termination through windows giving rise to two-periodic motion near $\Omega = 0.5387$

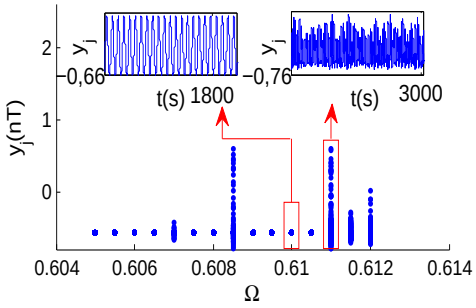

Fig. 32: Transition from a periodic response to chaotic motion near $\Omega = 0.611$

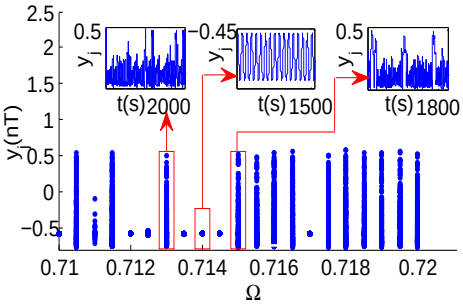

Fig. 33: Termination of chaos through windows leading to one periodic motion near Ω=0.714

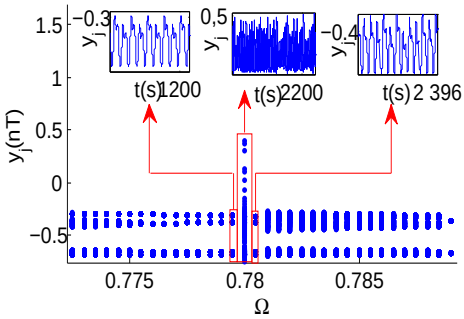

Fig. 34: Transition to a bi-periodic regime through Period-halving near Ω=0.781

4.3 Analysis of Nonlinear Forced Responses

The nonlinear response of the controlled system is analyzed through the forced response curves (FRCs) for different values of the proportional feedback gain P, derivative D and coupling α.

As presented in Figure 35, the FRC response is plotted for $P \in \{2.5, 2, 1.5, 1.1\}$, For $P = 2.5$, the system exhibits a strongly nonlinear response. The FRC displays a pronounced leftward branch, indicating a dominant softening-type nonlinearity, with a maximum amplitude of 1.317 at $\Omega = 0.37$. The bifurcation diagram as presented in Figure 39 shows a wide frequency interval $\Omega \in [0.24, 0.43]$ devoid of stable periodic solutions.

For $P = 2$, the nonlinear characteristics remain significant. The FRC retains a clear softening behavior, with a peak amplitude of 1.22 at $\Omega = 0.411$. The bifurcation diagram reveals a reduced gap in the interval $\Omega \in [0.29, 0.41]$ as illustrated in Figure 38,

indicating that the frequency range associated with instability of periodic solutions decreases as P is reduced, although quasi-periodic responses persist.

At $P = 1.5$, the system exhibits weakly nonlinear behavior. The FRC shows only a slight deviation from linearity, with a maximum amplitude of 0.87 at $\Omega = 0.412$. However, the bifurcation diagram indicates a narrow interval $\Omega \in [0.34, 0.38]$ as presented in Figure 37 where periodic solutions lose stability.

For $P = 1.1$, the FRC appears nearly linear, with a maximum amplitude of approximately 0.67 at $\Omega = 0.42$. Nevertheless, the bifurcation analysis as shown in Figure 36 reveals the presence of nonlinear dynamics, including multiharmonic, quasi-periodic, and intermittent chaotic responses, without any gap in the considered frequency range. This indicates that the system already operates in a weakly nonlinear regime despite the apparent linearity of the FRC.

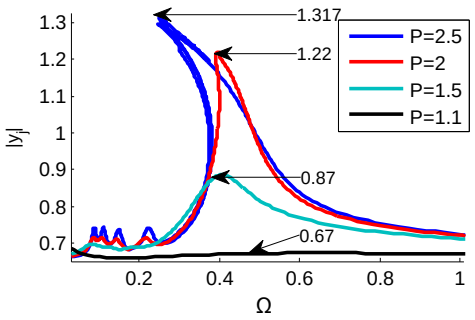

Fig. 35: FRC responses for $P \in \{2.5, 2, 1.5, 1.1\}$

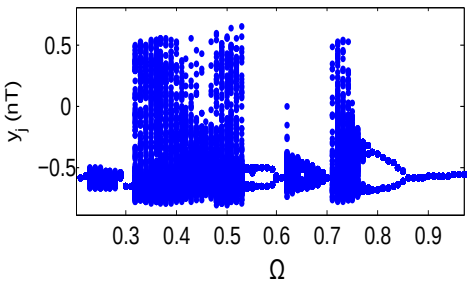

Fig. 36: Bifurcation diagram for $P = 1.1$

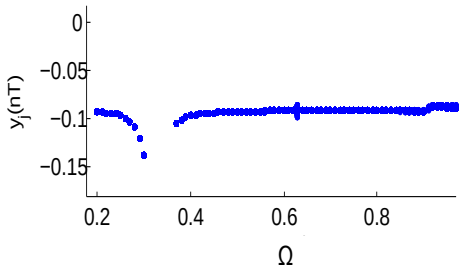

Fig. 37: Bifurcation diagram for $P = 1.5$

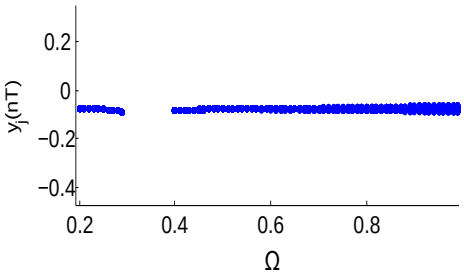

Fig. 38: Bifurcation diagram for $P = 2$

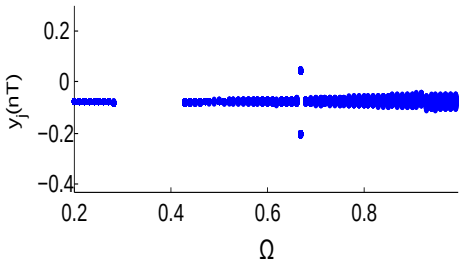

Fig. 39: Bifurcation diagram for P=2.5

The influence of the derivative feedback gain D on the system dynamics is also investigated through the forced response curves (FRCs) as presented in Figure 40.

For $D = 0.03$, the system exhibits a strongly nonlinear response. The FRC is significantly bent toward lower frequencies, reflecting a dominant softening-type behavior, with a maximum amplitude of 1.317 at $\Omega = 0.37$. The bifurcation diagram reveals Figure 41 an extended frequency interval $\Omega \in [0.24; 0.43]$ where periodic solutions are not sustained, and the dynamics are mainly governed by quasi-periodic motion.

Increasing the gain to $D = 0.05$ reduces the intensity of the nonlinear effects. The FRC still shows a softening branch, with a reduced peak amplitude of 1.15 at $\Omega = 0.40$. The corresponding bifurcation diagram Figure 42 indicates a contraction of the non-periodic region to $\Omega \in [0.30, 0.39]$, while periodic and quasi-periodic behaviors coexist near the transition boundaries.

At D=0.1, the response becomes closer to linear. The FRC exhibits only a mild deviation from linearity, with a maximum amplitude of 0.86 at $\Omega = 0.44$. The bifurcation diagram Figure 43 shows a very limited interval $\Omega \in [0.37, 0.39]$ where periodic solutions lose stability, indicating that the system response is predominantly single-periodic outside this narrow band.

For D=0.5, the FRC is almost linear, with a maximum amplitude of approximately 0.65 at $\Omega = 0.45$. The bifurcation diagram Figure 44 confirms the absence of any instability regions, and the response remains entirely single-periodic over the studied frequency range.

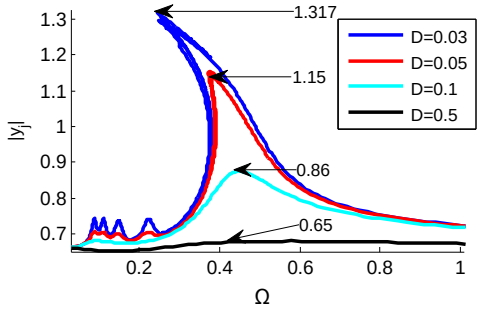

Fig. 40: FRC responses for $D \in \{0.03, 0.05, 0.1, 0.5\}$

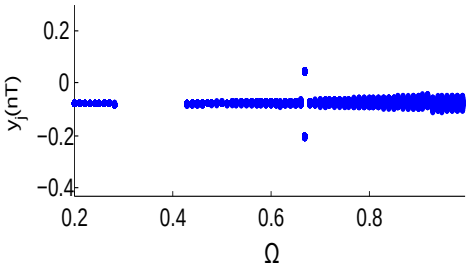

Fig. 41: Bifurcation diagram for $D = 0.03$

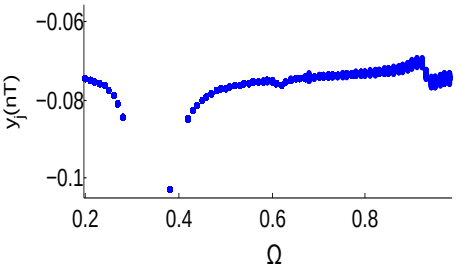

Fig. 42: Bifurcation diagram for $D = 0.05$

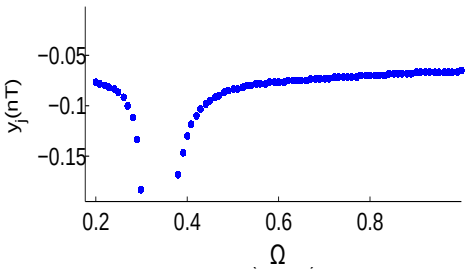

Fig. 43: Bifurcation diagram for $D = 0.1$

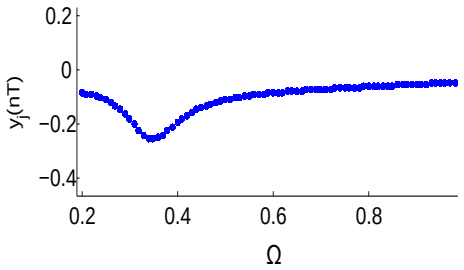

Fig. 44: Bifurcation diagram for $D = 0.5$

The influence of the electromagnetic coupling coefficient α on the system dynamics is investigated through the forced response curves (FRCs) as shown in Figure 50, 49, 46 and 45 and the associated bifurcation diagrams over the frequency range $\Omega \in [0; 1]$.

For $\alpha = 1$, the system exhibits a strongly nonlinear response. The FRC presents multiple inclined branches, indicating pronounced softening-type behavior, with a maximum amplitude of 1.239 at $\Omega = 0.23$ (Figure 50). The bifurcation diagram as shown in Figure 52 reveals several frequency intervals where periodic solutions are not sustained, namely $\Omega \in [0.22; 0.43], [0.57; 0.59], [0.815; 0.823]$. In contrast, stable periodic responses are observed in the ranges $\Omega \in [0.20; 0.22], [0.43; 0.57]$. Transitions toward biperiodic responses occur around $\Omega = 0.42$ and within $[0.59; 0.60]$, while the remaining regions are predominantly characterized by quasi-periodic dynamics, with an additional biperiodic window near $\Omega = 0.81$.

When the coupling is reduced to $\alpha = 0.5$, the number of nonlinear branches in the FRC decreases, although the softening behavior remains evident. The maximum amplitude slightly increases to 1.29 at $\Omega = 0.23$ (Figure 49). The bifurcation diagram as shown in Figure 51 shows a contraction of the main non-periodic interval to $\Omega \in [0.26, 0.43]$. A transition from periodic to biperiodic motion is observed in the range $[0.62, 0.64]$, after which the response becomes predominantly quasi-periodic, with a localized biperiodic regime near $\Omega = 0.92$.

For $\alpha = 0.03$, the system still exhibits nonlinear behavior but with fewer branches. The FRC shows two closely spaced nonlinear branches, with a maximum amplitude of 1.315 at $\Omega = 0.248$ (Figure 46). The bifurcation diagram indicates as shown in Figure 48 a reduced instability interval $\Omega \in [0.28, 0.43]$, accompanied by a biperiodic response around $\Omega = 0.64$, followed by a quasi-periodic regime.

At $\alpha = 0.01$, the FRC simplifies further, exhibiting essentially a single nonlinear branch, with a maximum amplitude of approximately 1.338 at $\Omega = 0.256$ (Figure 45). The bifurcation diagram as shown in Figure 47 confirms a narrower instability interval $\Omega \in [0.32, 0.43]$. Outside this region, the response remains predominantly single-periodic, with the exception of a localized higher-period response (period-4) near $\Omega = 0.68$.

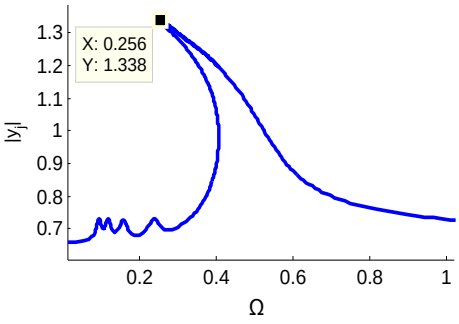

Fig. 45: FRC responses for $\alpha = 0.01$

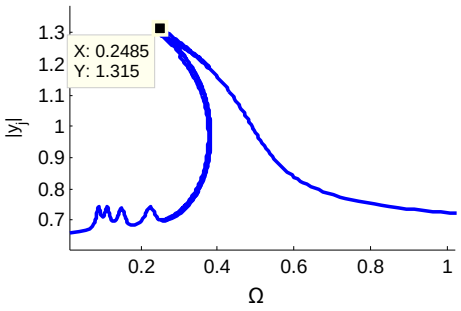

Fig. 46: FRC responses for $\alpha = 0.03$

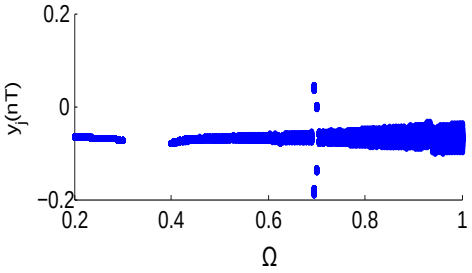

Fig. 47: Bifurcation diagram for $\alpha = 0.01$

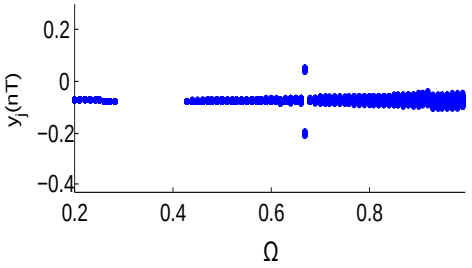

Fig. 48: Bifurcation diagram for $\alpha = 0.03$

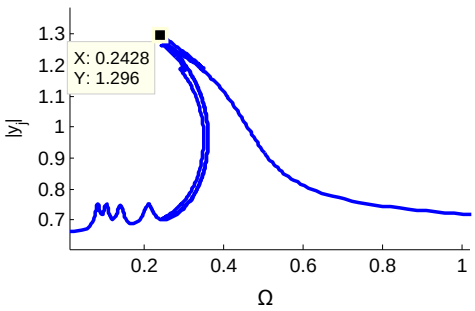

Fig. 49: FRC responses for $\alpha = 0.5$

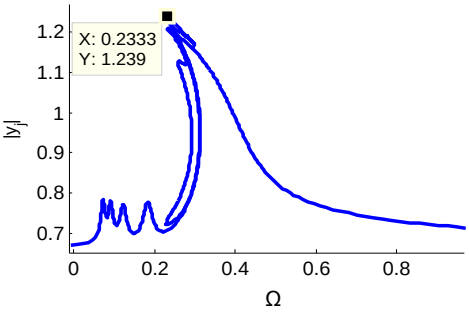

Fig. 50: FRC responses for $\alpha = 1$

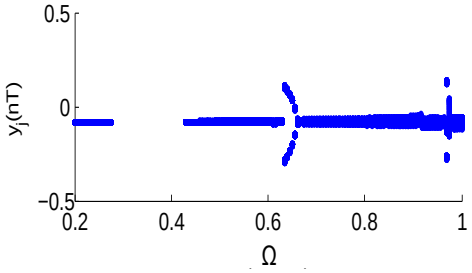

Fig. 51: Bifurcation diagram for $\alpha = 0.5$

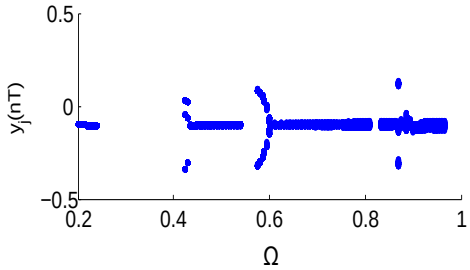

Fig. 52: Bifurcation diagram for $\alpha = 1$

The combined influence of the proportional gain P, derivative gain D, and electromagnetic coupling coefficient α reveals distinct and complementary roles in shaping the nonlinear dynamics of the system.

The proportional gain P primarily acts as a destabilizing parameter that enhances nonlinear effects. Increasing P leads to pronounced softening behavior in the FRCs, the emergence of multivalued and inclined branches, and the expansion of frequency intervals in the bifurcation diagrams where periodic solutions lose stability. This results in strong multistability and the proliferation of quasi-periodic and chaotic responses, indicating a significant restructuring of the system's phase space.

In contrast, the derivative gain D exhibits a stabilizing influence on the dynamics. As D increases, the nonlinear features progressively vanish, the FRCs become less distorted, the number of nonlinear branches decreases, and the frequency intervals associated with instability shrink and eventually disappear. For sufficiently large D, the system response becomes predominantly single-periodic, demonstrating the damping-like effect of derivative feedback in suppressing complex oscillatory regimes.

The electromagnetic coupling coefficient α plays an intermediate but crucial role by modulating the strength of nonlinear interactions. Higher values of α promote the appearance of multiple nonlinear branches in the FRCs and enlarge the regions of quasi-periodic and higher-order periodic responses in the bifurcation diagrams. Conversely, decreasing α leads to a progressive simplification of the response, characterized by fewer nonlinear branches and reduced instability intervals, with a tendency toward stable periodic motion.

5 Discussion

The numerical results reveal a rich nonlinear dynamical behavior arising from the interplay between structural flexibility, electromagnetic actuation, and proportional–derivative feedback control. Rather than acting independently, the three governing parameters, proportional gain P, derivative gain D, and electromagnetic coupling coefficient α interact to collectively shape the bifurcation structure, the nature of resonance, and the routes between periodic, quasi-periodic, and chaotic regimes. Understanding their individual and combined roles provides both physical insight and practical guidance for the design of feedback-controlled rotating machinery.

The proportional gain acts primarily as a stiffness-modifying parameter. Increasing P reduces the effective restoring force of the magnetic bearing system, pushing the journal displacement deeper into the nonlinear region of the electromagnetic force characteristic. This manifests physically as a pronounced softening-type nonlinearity in the forced response curves, with increasing bending of solution branches toward lower frequencies and the emergence of multivalued amplitude regions. The bifurcation diagrams confirm that higher values of P widen the frequency intervals over which periodic solutions lose stability, giving rise to quasi-periodic and chaotic attractors. These findings extend the observations of Cole et al. [5] and Kuperman [8], who reported amplified resonance under proportional feedback in simpler rotor-bearing configurations, to the case of a flexible rotor with coupled electromagnetic actuation, a configuration not addressed in those earlier works. The present results therefore suggest that proportional gain should be treated as a primary risk factor for dynamic instability in electromagnetically controlled rotor systems.

While the proportional gain drives the system toward complex behavior, the derivative gain plays the opposite role by introducing a velocity-proportional dissipative mechanism that acts analogously to viscous damping in the bearing force. As D increases, energy is progressively extracted from oscillatory modes, which widens the basin of attraction of stable periodic solutions and suppresses the secondary bifurcations responsible for quasi-periodic and chaotic motion. This is reflected in the forced response curves by a systematic reduction in branch distortion, a contraction of instability intervals in the bifurcation diagrams, and the eventual recovery of globally single-periodic behavior for sufficiently large D. This stabilizing role is consistent with the findings of Inayat-Hussain [13] and Chinta and Palazzolo [18], who demonstrated that derivative action in PD-controlled magnetic bearings effectively counteracts nonlinear instabilities. The present parametric study quantifies this effect more precisely by identifying the threshold derivative gain beyond which instability regions vanish entirely, offering a concrete design criterion for practical applications.

Beyond the controller gains, the electromagnetic coupling coefficient α governs the strength of cross-axis interaction between the horizontal and vertical bearing force components. Physically, higher values of α enhance energy exchange between the two lateral degrees of freedom, promoting modal interaction and enabling the system to sustain torus-type attractors associated with quasi-periodic motion. This is evidenced by the multiplication of nonlinear solution branches in the forced response curves and the enlargement of quasi-periodic regions in the bifurcation diagrams as α increases. Conversely, reducing α weakens this inter-axis coupling, simplifying the response toward single-branch periodic behavior. This finding highlights a design implication that has not been explicitly addressed in the existing literature: the geometric coupling parameter of the magnetic bearing, which determines α, constitutes an additional passive tuning lever for the nonlinear dynamic behavior, independent of the feedback controller gains.

Concerning the transition mechanisms, the identified scenarios, direct periodic-to-chaotic windows, period-halving sequences, and chaotic phases bounded by narrow periodic windows are characteristic of intermittency and boundary crisis mechanisms rather than the classical period-doubling cascade associated with the Feigenbaum route. In a boundary crisis, the chaotic attractor collides with an unstable periodic orbit at the boundary of its basin of attraction, causing an abrupt onset or termination of chaos without gradual precursors. This distinction carries a practical consequence, unlike period-doubling cascades, which provide observable warning signals through successive subharmonic growth, crisis-induced chaos can appear suddenly as an operating parameter crosses a critical threshold. In the context of rotating machinery, this implies that monitoring subharmonic content alone may be insufficient for early detection of impending chaotic operation, and that broader spectral surveillance strategies should be considered.

Regarding the computational framework, the Harmonic Quadrature Method combined with arc-length continuation demonstrated robust performance across all tested configurations. The method successfully tracked unstable solution branches, detected fold bifurcations, and resolved multistable regions that conventional frequency-sweep integration and time-domain shooting methods failed to capture, as confirmed by the

validation cases against Chinta and Palazzolo [18] and Inayat-Hussain [26]. Convergence was achieved consistently with $H = 11$ harmonics, which represents a moderate computational cost compared to direct time integration over long transients. The arc-length constraint proved particularly effective in the vicinity of turning points, where conventional incremental techniques diverge. These properties suggest that the proposed framework is well suited for systematic parametric studies of strongly nonlinear rotor systems, including configurations with multiple coupled degrees of freedom.

Finally, the present study is subject to several simplifying assumptions that define the boundaries of its applicability. Gyroscopic effects, which become significant at high rotational speeds, have been neglected in the model formulation. The lumped-mass idealization of the rotor may not fully capture the distributed flexibility of long or geometrically complex shafts. Furthermore, the analysis is restricted to steady-state periodic responses under constant rotational speed, and transient dynamics during run-up, coast-down, or sudden load changes are not addressed. Quantitative chaos indicators such as Lyapunov exponents have not been computed, and the stability classification of solution branches relies on indirect evidence from bifurcation diagrams rather than formal Floquet analysis. Future work should incorporate these elements, and may further extend the HQM continuation framework to systems involving multi-mode interactions, parametric excitations arising from magnetic misalignment, bearing asymmetry, and more complex actuator geometries representative of industrial magnetic bearing designs.

6 Conclusion

The nonlinear dynamics of an electromagnetically controlled rotor system under proportional-derivative feedback have been investigated using bifurcation diagrams, FFT spectra, Poincaré sections, phase portraits, and forced response curves computed via an extended Harmonic Quadrature Method with arc-length continuation.

The system exhibits a wide spectrum of dynamical behaviors, including periodic, period-doubled, higher-order periodic, quasi-periodic, and chaotic responses, depending on the excitation frequency and control parameters. Multiple disjoint parameter intervals corresponding to each dynamical regime have been identified and characterized. The proportional gain P enhances nonlinear effects, leading to pronounced softening behavior, multistability, and expanded quasi-periodic regions in the bifurcation diagrams. Increasing P widens the frequency intervals over which periodic solutions lose stability. The derivative gain D acts as a stabilizing parameter by introducing effective damping. Sufficiently large values of D suppress nonlinear distortions, eliminate instability regions, and restore single-periodic motion across the entire frequency range. The electromagnetic coupling coefficient α modulates the intensity of nonlinear interactions. Higher values promote multiple solution branches and complex oscillatory regimes, while lower values simplify the response toward periodic behavior. The routes to chaos proceed through windows of chaotic motion embedded between periodic regimes, with quasi-periodic states acting as intermediate transitions. Chaotic phases terminate through narrow windows leading to stabilized periodic responses. The HQM-based arc-length continuation framework provides an efficient and accurate

computational tool for tracking nonlinear solution branches, detecting multistability, and characterizing complex resonance phenomena in controlled rotor dynamics.

These results provide a comprehensive understanding of the nonlinear mechanisms governing electromagnetically controlled rotor systems and offer practical guidelines for the design and tuning of feedback-controlled rotating machinery.

Acknowledgements

The authors would like to thank the Applied Mechanics and Systems Research Laboratory for providing the research environment and computational resources used in this work.

Author Contributions

All authors contributed to the study conception and design. data collection and analysis were performed by Farouk Thaljaoui, Thabet Guesmi and Wathek Thaljaoui. The first draft of the manuscript was written by Farouk Thaljaoui and all authors commented on previous versions of the manuscript. All authors read and approved the final manuscript.

Funding

No funding was received to assist with the preparation of this manuscript.

Declarations

- **Data Availability** Data used in this study were obtained from previously published works cited in the manuscript.
- **Code Availability** The code used in this study is proprietary and available upon reasonable request.
- **Conflict of Interest** The authors declare that they have no conflicts of interest.

References

[1] Farouk Thaljaoui, Mohamed Trabelssi, and Molka Hili. Implementation of a new approach based on harmonic quadrature method on the study of a misaligned rotor supported in ball bearings squeeze film system. In Ali Akrout, Moez Abdennadher, and Nabih Feki, editors, *Applied Condition Monitoring*, volume 22, pages 328–341, Tunisia, 2022. Springer.

[2] Farouk Thaljaoui, Molka Hili, and Mohamed Trabelssi. Nonlinear multi-harmonic response of a misaligned rotor under base vibration motion using the harmonic quadrature method. *Journal of the Brazilian Society of Mechanical Sciences and Engineering*, 47(7), 2025.

[3] Lei Hou, Huizheng Chen, Yushu Chen, Kuan Lu, and Zhansheng Liu. Bifurcation and stability analysis of a nonlinear rotor system subjected to constant excitation and rub-impact. *Mechanical Systems and Signal Processing*, 125:65–78, 2018.

[4] Tianzhu Wang and Qian Ding. Nonlinear normal modes and dynamic balancing for a nonlinear rotor system. *Nonlinear Dynamics*, 112:10823–10844, 2024.

[5] M. O. T. Cole, P. S. Keogh, and C. R. Burrows. Vibration control of a flexible rotor/magnetic bearing system subject to direct forcing and base motion disturbances. *Proceedings of the Institution of Mechanical Engineers, Part C: Journal of Mechanical Engineering Science*, 212:535–546, 1998.

[6] J. C. Ji, Colin H. Hansen, and Anthony C. Zander. Nonlinear dynamics of magnetic bearing systems. *Journal of Intelligent Material Systems and Structures*, 19:1471–1491, 2008.

[7] I. Sina Kuseyri. Robust control and unbalance compensation of rotor/active magnetic bearing systems. *Journal of Vibration and Control*, 18:817–832, 2011.

[8] Alon Kuperman. Uncertainty and disturbance estimator-assisted control of a two-axis active magnetic bearing. *Transactions of the Institute of Measurement and Control*, 38:764–772, 2016.

[9] Lingchun Li, Huimin Ouyang, Meiying Ou, and Laixin Gao. Sliding mode control of active magnetic bearing rotor system based on state observer. *Advances in Mechanical Engineering*, 16, 2024.

[10] Hanqing Guan, Jiajun Li, Kexiang Wei, Shenggui Chu, Yueqi Guan, and Changyun Wen. Dynamics and adaptive backstepping control of rotor-hybrid foil-magnetic bearings system. *Journal of Vibration and Control*, 31:3553–3567, 2024.

[11] Hang Zhang, Miaomiao Cheng, Xiang Zhou, Libo Feng, and Kai Feng. Investigations on the nonlinear dynamic characteristics of a rotor supported by hybrid foil magnetic bearings. *Nonlinear Dynamics*, 111:14879–14899, 2023.

[12] J. C. Ji and C. H. Hansen. Non-linear oscillations of a rotor in active magnetic bearings. *Journal of Sound and Vibration*, 240:599–612, 2001.

[13] Jawaid I. Inayat-Hussain. Nonlinear dynamics of a magnetically supported rigid rotor in auxiliary bearings. *Mechanism and Machine Theory*, 45:1651–1667, 2010.

[14] Aboozar Heydari, Mina Mirparizi, Farshad Shakeriaski, Farhad Sheykh Samani, and Mohamadreza Keshavarzi. Nonlinear vibration analysis of a rotor supported by magnetic bearings using homotopy perturbation method. *Propulsion and Power Research*, 6:223–232, 2017.

[15] Reza Ebrahimi, Mostafa Ghayour, and Heshmatallah Mohammad Khanlo. Nonlinear dynamic analysis and experimental verification of a magnetically supported flexible rotor system with auxiliary bearings. *Mechanism and Machine Theory*, 121:545–562, 2018.

[16] R. D. Smith and W. F. Weldon. Nonlinear control of a rigid rotor magnetic bearing system: modeling and simulation with full state feedback. *IEEE Transactions on Magnetics*, 31:973–980, 1995.

[17] Hiroki Gotanda, Ryousuke Amano, and Toshihiko Sugiura. Mode coupling of a flexible rotor supported by a superconducting magnetic bearing due to the nonlinearity of electromagnetic force. *IEEE Transactions on Applied Superconductivity*, 21:1481–1484, 2011.

[18] M. Chinta and A. B. Palazzolo. Stability and bifurcation of rotor motion in a magnetic bearing. *Journal of Sound and Vibration*, 214:793–803, 1998.

[19] H. J. Holl. An efficient semi-analytic time integration method with application to non-linear rotordynamic systems. *Computational Mechanics*, 26:362–375, 2000.

[20] Jie Wu, Xianbin Du, Yijiang Ma, and Peng Ren. Research of precise time integration method and its derived formats on helicopter rotor dynamics. *International Journal of Computational Methods*, 17:1950059, 2019.

[21] P. Sundararajan and S. T. Noah. Dynamics of forced nonlinear systems using shooting/arc-length continuation method — application to rotor systems. *Journal of Vibration and Acoustics*, 119:9–20, 1997.

[22] T. Zheng and N. Hasebe. Nonlinear dynamic behaviors of a complex rotor-bearing system. *Journal of Applied Mechanics*, 67:485–495, 1999.

[23] Haiyang Luo and Yuefang Wang. Nonlinear dynamics analysis of a continuum rotor through generalized harmonic balance method. *Journal of Applied Nonlinear Dynamics*, 5:1–31, 2016.

[24] J. Didier, J.-J. Sinou, and B. Faverjon. Multi-dimensional harmonic balance with uncertainties applied to rotor dynamics. *Journal of Vibration and Acoustics*, 134:485–495, 2012.

[25] Min Sun and Jianen Chen. Dynamics of nonlinear primary oscillator with nonlinear energy sink under harmonic excitation: effects of nonlinear stiffness. *Mathematical Problems in Engineering*, 2018:1–13, 2018.

[26] Jawaid I. Inayat-Hussain. Bifurcations of a flexible rotor response in squeeze-film dampers without centering springs. *Chaos, Solitons & Fractals*, 24:583–596, 2004.